Nanodomains in multiferroic hexagonal $R\mathrm{MnO_3}$ films (R=Y,Dy,Ho,Er)

T. Kordel, C. Wehrenfennig, D. Meier, Th. Lottermoser, and M. Fiebig
HISKP, Universität Bonn, Nussallee 14-16, 53115 Bonn, Germany

I. Gélard and C. Dubourdieu
Laboratoire des Matériaux et du Génie Physique, CNRS, Grenoble INP, 3 parvis L. Néel, 38016 Grenoble, France

J.-W. Kim, L. Schultz, and K. Dörr
Institute for Metallic Materials, IFW Dresden, Postfach 270116, 01171 Dresden, Germany
(Received 17 February 2009; revised manuscript received 30 May 2009; published 13 July 2009)

A homogeneous distribution of ferroelectric nanoinclusions was observed by optical second harmonic generation in epitaxial films of hexagonal $R\mathrm{MnO_3}$ (R=Y,Dy,Ho,Er) grown on $ZrO_2(Y_2O_3)$ substrates. The inclusions correspond to secondary orientations in the c-axis-oriented films. Their volume density is in the range of 10^{-3} and their occurrence is independent of growth technique and film thickness in the range of 20–1000 nm. The inclusions behave as preferentially polarized ferroelectric nanodomains whereas the epitaxial film is in a ferroelectric single-domain state. In addition, the antiferromagnetic phase exhibits nanodomains of $<$100 nm which is three orders of magnitude below the extension of bulk antiferromagnetic domains in $R\mathrm{MnO_3}$. Indications for a polarization-induced magnetic order different from that of the bulk are discussed.

DOI: 10.1103/PhysRevB.80.045409 PACS number(s): 68.55.Ln, 77.80.Dj, 75.50.Ee, 42.65.Ky

I. INTRODUCTION

In the search for novel multifunctional devices manipulation of the magnetic properties by an electric field (or vice versa) is an important challenge. Compounds with a coexistence of magnetic and ferroelectric order called multiferroics display a particularly rich variety of magnetoelectric cross-coupling phenomena.[1–3] This includes magnetoelectric, magnetodielectric, magnetocapacitive effects, and magnetically induced ferroelectricity in spin-spiral compounds. Most spectacular is the induction of electric phase transitions by magnetic fields, such as in orthorhombic $TbMnO_3$,[4] and the induction of magnetic phase transitions by electric fields observed, e.g., in hexagonal $HoMnO_3$.[5]

Among the boosting number of publications on multiferroics, the share devoted to the multiferroic properties of thin films is still relatively small and restricted to a narrow choice of compounds with most of the activity being focused on $BiFeO_3$.[6] However, in comparison to bulk crystals, thin films offer powerful advantages from the point of view of basic research as well as technological applications. Films can be structured on the nanometer scale and additional degrees of freedom, such as the composition, orientation, and substrate stress are available for extending the phase diagram of the film beyond that of the bulk compound. From this perspective, hexagonal $R\mathrm{MnO_3}$ is particularly interesting because with R=Sc, Y, In, and Sm-Lu, the range of compounds grown as bulk crystal and/or thin film is very broad, which is beneficial in the investigation of general criteria determining the multiferroic properties. In addition, the hexagonal $R\mathrm{MnO_3}$ system revealed giant manifestations of magnetoelectric coupling.[5,7,8]

The magnetic phase diagram of the $R\mathrm{MnO_3}$ bulk compounds and the interaction between magnetic and the ferroelectric order are well known. Ferroelectric ordering occurs in a two-stage transition[9,10] with a Curie temperature T_C of 570–990 K and a spontaneous polarization of 5.6 $\mu\mathrm{C/cm^2}$.[11,12] The crystallographic space symmetry of the ferroelectric state is $P6_3cm$. For its description, we use a Cartesian coordinate system which is related to the hexagonal unit-cell axes by $z=c$ and $x=a$. At a Néel temperature T_N between 60 and 130 K, antiferromagnetic ordering of the magnetic Mn^{3+} spins occurs in the basal plane perpendicular to the sixfold z axis.[13,14] The spins are oriented along the x or y axis in a triangular fashion with $P6_3c\underline{m}$ or $P6_3\underline{c}m$, respectively, as magnetic space symmetry.[15,16] At a temperature T_{RE} between 4 and 8 K, additional magnetic R^{3+} ordering with reordering of the Mn^{3+} spins occurs in the compounds with partially filled $4f$ shell which changes the magnetic symmetry further.[17] $HoMnO_3$ may be the most challenging of the hexagonal $R\mathrm{MnO_3}$ multiferroics because of its complex phase transitions.[18] We have T_C=875 K, T_N=76 K, and T_{RE}=5 K. In addition, between 50 and 30 K, a collective 90° rotation of the Mn^{3+} spins from the y to the x axis changes the magnetic symmetry from $P6_3\underline{c}m$ above the transition to $P6_3c\underline{m}$ below the transition. An electric field of 10^5 V/cm applied at sufficiently high temperature transforms the sample into a ferroelectric single-domain state which induces ferromagnetic Ho^{3+} ordering below T_N via the linear magnetoelectric effect.[5]

Hexagonal $YMnO_3$ was the first magnetic ferroelectric ever grown as thin film.[12] Other compounds with R=Sm-Er were also realized.[19–30] For R=Sm-Dy, the hexagonal phase was obtained by epitaxial phase stabilization whereas the preferred configuration is the orthorhombic one.[19–21] The hexagonal phase is stabilized up to a thickness of several tens of nm.

Investigations were mostly focused on comparing the properties of the films to those of the corresponding bulk compounds. Surprisingly, even at a film thickness of 150 nm, the hexagonal lattice constants differ by 0.1–1 % from the bulk values. In the dielectric properties, a reduction in the spontaneous polarization by about 50% and, in some cases, a tendency for antiferroelectric poling behavior was

observed.[22–24] In the magnetic properties, a decrease in the antiferromagnetic ordering temperature of the Mn^{3+} lattice by 10–20 % was observed by magnetization measurements[22,24] and neutron diffraction[25] except for $HoMnO_3$, where neutron diffraction revealed a single magnetic transition at 50 K.[25]

In summary, investigations on hexagonal $RMnO_3$ films thus far were either restricted to atomic resolution within the lateral extent of a few unit cells or to integral techniques probing the samples on a macroscopic length scale. Properties and ordering phenomena, such as domain structures and antiphase boundaries affecting the "nanoscopic" range from ~50 nm to 1 μm, were neglected. Yet, these aspects determine qualities such as conductivity, leakage currents, magnetoelectric effects, and field-poling behavior that are vital for device applications.

Here, we investigate epitaxial hexagonal $RMnO_3$ films by optical second harmonic generation (SHG). We find that throughout the films, inclusions with secondary crystallographic orientations are formed independent of growth technique and film thickness. The inclusions have a lateral size of $\ll 1$ μm and they behave as ferroelectric nanodomains with a preferred crystallographic orientation of their spontaneous polarization. The volume density of the nanodomains is in the range of 10^{-3}. Their preferential orientation comes along with a ferroelectric single-domain state of the surrounding epitaxial *c*-oriented film "matrix." Antiferromagnetic domains have a lateral extension of <100 nm and are thus at least two orders of magnitude smaller than in bulk samples. Most of the data shown here refer to $HoMnO_3$ as the best-known constituent of the $RMnO_3$ series, but other constituents were included as mentioned in the text.

II. EXPERIMENT

A variety of $RMnO_3$ compounds, growth types, and values of film thickness were compared. On the one hand, films with $R=Y,Dy,Ho,Er$ were grown on (111) oriented $ZrO_2:Y_2O_3$(YSZ) by liquid-injection metal organic chemical vapor deposition (MOCVD) at the CNRS in Grenoble.[31] They possessed a thickness of 50–650 nm. On the other hand, films with $R=Y,Ho$ and a thickness of 20–1000 nm were grown on YSZ(111) by pulsed-laser deposition (PLD) at the IFW in Dresden.[32] The substrates had been polished on both sides for optical transmission experiments. The quality of all films was analyzed by x-ray diffraction. The $\theta-2\theta$ diffractograms, rocking curves, and pole figures indicated epitaxial hexagonal and *z*-oriented growth of the films. The epitaxial relationships are $(111)_{YSZ}\|(001)_{RMnO_3}$ and $\langle 1\bar{1}0\rangle_{YSZ}\|\langle 1\bar{1}0\rangle_{RMnO_3}$, using cubic unit vectors for the substrate and hexagonal unit vectors for the film.

The ferroic structure of the $RMnO_3$ films was investigated by optical SHG described by the equation[33]

$$P_i(2\omega) = \varepsilon_0 \chi_{ijk} E_j(\omega) E_k(\omega). \quad (1)$$

Here $\vec{E}(\omega)$ is the electric field of an incident light wave at frequency ω. It induces the nonlinear polarization $\vec{P}(2\omega)$ in the sample, which acts as the source of a frequency-doubled light wave. The tensor $\hat{\chi}$ denotes the nonlinear susceptibility. Following the Neumann principle, the symmetry of the sample determines the set of tensor components $\chi_{ijk} \neq 0$ (with $i,j,k \in \{x,y,z\}$). Each form of ferroic order affects the symmetry in a different way so that there will be SHG contributions coupling to the ferroelectric and the antiferromagnetic order, respectively, that can be separated by polarization analysis.[34] The SHG contributions for hexagonal $RMnO_3$ are listed in Table I. Antiferromagnetic contributions to SHG involve *x*-polarized and *y*-polarized light only while for all ferroelectric contributions, at least one *z*-polarized light wave contributes. Hence, the antiferromagnetic order is best observed with light incident along the *z* axis, where ferroelectric SHG contributions cannot be excited. In turn, an investigation of the ferroelectric order is only possible with light *not* incident along the *z* axis. Here, mixing with antiferromagnetic contributions to SHG is avoided by a suitable choice of polarizations or by performing the experiment at $T > T_N$ where the antiferromagnetic SHG contribution is zero.

TABLE I. Tensor components for SHG in hexagonal $HoMnO_3$ according to Eq. (1) and Ref. 36 using Cartesian coordinates.

Space symmetry	SHG tensor components
	Ferroelectric
$P6_3cm$	χ_{zzz}, $\chi_{zxx}=\chi_{zyy}$, $\chi_{xxz}=\chi_{yyz}$
	Antiferromagnetic
$P6_3\underline{c}m$	$\chi_{xxx}=-\chi_{xyy}=-\chi_{yxy}=-\chi_{yyx}$
$P6_3c\underline{m}$	$\chi_{yyy}=-\chi_{yxx}=-\chi_{xyx}=-\chi_{xxy}$

Two types of laser systems, a Nd:YAG laser-generating 3 ns light pulses and a Ti:sapphire laser-generating 130 fs light pulses, were used for the SHG experiments. Frequency-tripled light pulses at 10–40 Hz from the Nd:YAG laser were used to operate an optical parametric oscillator emitting light in the range of 0.5–3.0 eV. Amplified light pulses at 1 kHz from the Ti:sapphire laser were used to operate an optical parametric amplifier emitting light in the range of 0.45–2.25 eV. The linear polarization of light from either laser system was polarized by a half-wave plate and focused on the sample after higher harmonics generated in the optical components had been suppressed by optical long-pass filters. Samples were mounted in a liquid-helium cryostat that was operated in the range of 6–300 K. SHG was generated in transmission through the sample. It was separated from the fundamental light by optical short-pass filters and passed through a Glan prism for polarization analysis. It propagated through a monochromator suppressing two-photon luminescence, as well as scattered light, and was detected by a photomultiplier tube. Alternatively, the monochromator was removed and a liquid-nitrogen-cooled digital camera was used for spatially resolved detection.

III. RESULTS AND DISCUSSION

A. Origin of SHG in epitaxial $RMnO_3$ films

Figure 1 shows the polarization and the temperature dependence of the SHG intensity at 2.52 eV with fundamental

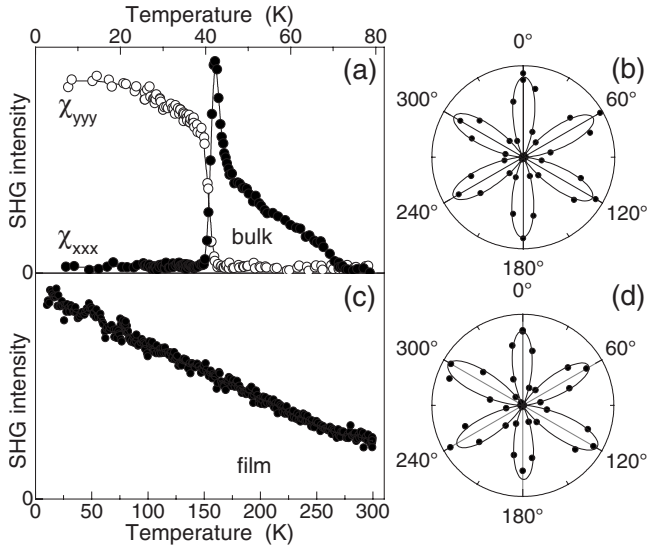

FIG. 1. Temperature-dependent and polarization-dependent SHG on $HoMnO_3$ bulk crystals and epitaxial films. (a) Temperature dependence of the SHG intensity from χ_{xxx} and χ_{yyy} from a flux-grown $HoMnO_3$ bulk sample for light incident along the z axis. The signal couples to the antiferromagnetic Mn^{3+} order. A spin reorientation at 40 K and the transition to the paramagnetic phase at 76 K are clearly visible. (b) Anisotropy of the SHG signal in (a) in the $P6_3\underline{c}m$ phase at 41 K$<T<$76 K. The x axis is set as 0°. (c) Temperature dependence of the SHG intensity from a $HoMnO_3$ film of 600 nm grown by PLD. The light is incident along the z axis of the epitaxial film and both the incident fundamental and the detected SHG light are x polarized. Even at 300 K, the SHG signal has not vanished. (d) Anisotropy of the SHG signal in (c). Solid lines in (b) and (d) are fits.

light incident along the z axis. Figures 1(a) and 1(b) were gained on a flux-grown $HoMnO_3$ bulk crystal, while Figs. 1(c) and 1(d) were obtained from epitaxial $HoMnO_3$ films of 600 nm grown by PLD and mounted in the cryostat along with the bulk crystal. [A plot as in Fig. 1(d) for a film grown by MOCVD is found in Fig. 4.] The anisotropy measurements in Figs. 1(b) and 1(d) were gained by detecting the component of the SHG light polarized parallel to the linear polarization of the incident fundamental light while rotating this polarization from 0° to 360°. Figure 1(b) reveals a polarization dependence with a sixfold symmetry which is fitted by $I^{\parallel}_{\mathrm{SHG}} \propto |\chi_{xxx}|^2 \sin^2(3\varphi)$ in agreement with the SHG tensor components in Table I for antiferromagnetic SHG in the $P6_3\underline{c}m$ symmetry group. At $T_R \approx 40$ K, this changes to $I^{\parallel}_{\mathrm{SHG}} \propto |\chi_{yyy}|^2 \cos^2(3\varphi)$ because of the change in magnetic symmetry from $P6_3\underline{c}m$ to $P6_3c\underline{m}$. At T_N, the SHG signal drops to zero because, as mentioned, no SHG signal is expected in the paramagnetic state for light incident along the z axis.[15]

The $HoMnO_3$ films reveal a polarization dependence that is similar to the polarization dependence of the bulk crystal, yet with a SHG intensity that is 1–2 orders of magnitude weaker than for the bulk sample. In Ref. 32, this was interpreted as indication for the antiferromagnetic order of the films, which are expected to exhibit a lower SHG yield because of their limited thickness. In the corresponding experiment, the SHG signal was taken with a nanosecond laser system and at the limit of detectability so that temperature-dependent and spectroscopic SHG measurements were impeded by the insufficient signal-to-noise ratio at short acquisition times and by long-term drifts of the experiment at long acquisition times. However, with the femtosecond laser systems available for the present experiment, a two-orders-of-magnitude higher SHG yield is obtained. Figure 1(c) shows the temperature dependence of SHG obtained on the $HoMnO_3$ film. At 300 K, the signal is 70% lower than at 10 K, but neither the spin reorientation at T_R nor the transition to the paramagnetic state at T_N are visible. In spite of the similarity of Figs. 1(b) and 1(d), this points against antiferromagnetic order as origin of the SHG signal in Fig. 1(d) because according to neutron diffraction, the $HoMnO_3$ films undergo a magnetic phase transition at 50 K.[25] Note that neutron diffraction on $YMnO_3$ and $ErMnO_3$ films revealed a deviation of the Néel temperature of only ~10% from the bulk value.

The following reasons for the emergence of a parasitic SHG signal were considered:

1. Multipole contributions to SHG

Apart from the electric-dipole-type polarization $\vec{P}(2\omega)$ in Eq. (1), higher-order multipole terms contribute to SHG.[35] The multipole expansion parameter is a/λ with a as lattice constant and λ as wavelength of the light. It is on the order of 10^{-3} so that only magnetic-dipole and electric-quadrupole contributions to SHG need to be considered. Derivation of these contributions on the basis of Ref. 36 reveals that both are zero for light incident along the z axis and cannot explain the SHG signal in Fig. 1(d).

2. Surface contributions to SHG

In general, a surface reduces the local symmetry of a crystal and leads to additional contributions to SHG. However, this is not the case for the symmetry group $P6_3cm$ and a surface oriented perpendicular to the z axis.

3. Substrate contributions to SHG

Substrates are crystalline and may, therefore, be a source for SHG even if they are centrosymmetric. Bulk substrate contributions are ruled out because in measurements on uncoated YSZ substrates, we did not obtain a SHG signal. Substrate-induced SHG may still arise at the YSZ/$R\mathrm{MnO_3}$ interface. For verification, we compared the SHG yield of a sample with either (i) the $HoMnO_3$ film or (ii) the substrate oriented toward the detector. In case (ii), any SHG signal emitted by the substrate passes through the $HoMnO_3$ film before it is detected and would, therefore, be attenuated in comparison to case (i). For a film of 200 nm and a photon energy $2\hbar\omega = 2.7$ eV, the transmission is only 15%. However, the same SHG intensity was observed for cases (i) and (ii) so that SHG contributions from the substrate can be excluded for Fig. 1(d).

4. Ferroelectric contributions to SHG

According to Table I and as mentioned before, ferroelectric contributions to SHG cannot be excited by light incident

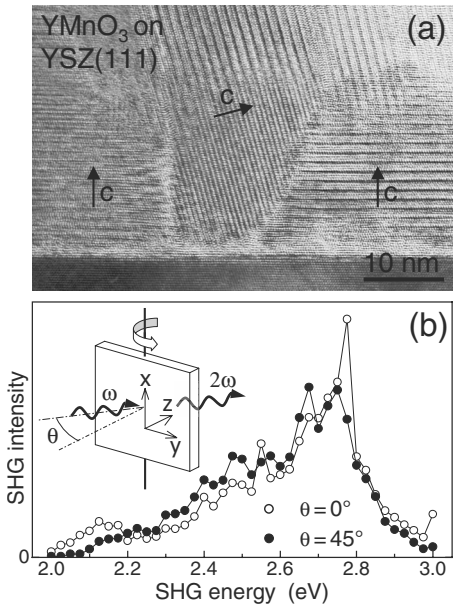

FIG. 2. Ferroelectric origin of SHG in the $R\mathrm{MnO_3}$ films. (a) HR-TEM image of a $\mathrm{YMnO_3}$ film grown by MOCVD. Nanoscopic inclusions with secondary crystallographic orientation are observed in intrinsically hexagonal $\mathrm{YMnO_3}$ films just as in epitaxially stabilized $R\mathrm{MnO_3}$ films (Ref. 21). (b) SHG spectra for a $\mathrm{HoMnO_3}$ film of 600 nm grown by PLD. The wave vector of the incident light includes an angle θ with the z axis of the crystal which was achieved by rotating the crystal as sketched in the inset. Filled symbols: SHG spectrum at 300 K for $\theta=45°$. Open symbols: SHG spectrum at 10 K for $\theta=0°$. Inset: geometry of the SHG experiment.

along the z axis. However, ferroelectric contributions are possible for regions (crystallites) with secondary orientations, whose crystallographic z axis is tilted with respect to the z axis of the epitaxial matrix. High-resolution transmission electron microscopy (HR-TEM), indeed, revealed the existence of such inclusions.[21] Thus far, they were only reported for "metastable" $R\mathrm{MnO_3}$ compounds in which the hexagonal phase is stabilized by the substrate up to a limited film thickness. Nevertheless, this observation is indicative so that the hypothesis of ferroelectric contributions to SHG in Fig. 1(c) is investigated in detail in Fig. 2.

First of all, HR-TEM data in Fig. 2(a) show that nanoscopic regions with secondary orientations are also observed in epitaxial films of the intrinsically hexagonal constituent $\mathrm{YMnO_3}$. This suggests that the formation of such crystallites is universal for hexagonal $R\mathrm{MnO_3}$ films and not related to the stabilization of crystallographically unfavorable phases.

Due to the local nature of HR-TEM, nothing is known about their global presence in the films. This aspect is pursued by SHG measurements in Fig. 2(b). The figure shows the spectral dependence of the SHG signal gained on the $\mathrm{HoMnO_3}$ film used in Fig. 1(c). Data were obtained at normal incidence ($\theta=0°$) and with the sample rotated by $\theta=45°$ around the x axis. Comparison with experiments done on bulk samples[37] reveals that the SHG signal observed on the rotated films is induced by their ferroelectric order. At $\theta=45°$, the z-polarized SHG contributions listed in Table I for the ferroelectric symmetry group $P6_3cm$ are accessible and in agreement with this, the intensity of the SHG signal increases with θ. The spectral dependence of this SHG signal resembles that of the ferroelectric signal in Ref. 37 and it possesses the same polarization dependence.

It is obvious that the SHG signal observed at $\theta=0°$ on the film yields the same spectral dependence as the ferroelectric bulk signal at $\theta=45°$ (the polarization dependence will be discussed in the following section). In addition to the room-temperature presence of the signal, this is a strong confirmation that SHG obtained on the $\mathrm{HoMnO_3}$ films with light along z is generated by ferroelectric inclusions with different crystallographic orientation.

B. Size and distribution of ferroelectric domains in $R\mathrm{MnO_3}$ films

Although crystalline inclusions may be regarded as undesired deviation from the ideal epitaxial state, the SHG signal emitted from these inclusions reveals valuable information about the nanostructure of the $R\mathrm{MnO_3}$ films. First of all, such crystallites are present in all hexagonal $R\mathrm{MnO_3}$ films investigated by us. We observed sample-to-sample variations within 1 order of magnitude in the density of the inclusions (indicated by the intensity of the corresponding SHG signal), but this could not be systematically related to the R compound, the growth technique, or the thickness. Within a film, the density of the inclusions does not vary. Even in a film with a thickness of 1000 nm, the density of the inclusions at the surface oriented toward the substrate and at the surface oriented toward air is the same. This was confirmed by SHG measurements at 2.7 eV which probe an (absorption-limited) region extending $\sim$100 nm into the film so that the two sides of the film can be probed independently. Both sides of the 1000 nm film revealed the same SHG intensity pointing to an equal density of nanocrystalline inclusions. The result shows that the formation of the inclusions is not a straightforward consequence of growth-induced strain imposed by the substrate because such strain relaxes with increasing distance from the substrate/film interface. It is possible that local strain generated by the misoriented nanoinclusion leads to the formation of further inclusions upon continued growth even up to 1 μm. In any case, even at a macroscopic thickness, the crystallographic properties of the hexagonal $R\mathrm{MnO_3}$ films do not approach the properties of the bulk crystal.[38]

Additional information about the size and distribution of the ferroelectric nanoinclusions is obtained from the polarization dependence of the SHG signal in the xy plane. According to the HR-TEM measurements, the inclusions are formed in the epitaxial c-oriented matrix with an orientation given as follows:[21] $(001)_{\mathrm{incl.}} \| (111)_{\mathrm{matrix}}$ and $\langle 1\bar{1}0\rangle_{\mathrm{incl.}} \| \langle 1\bar{1}0\rangle_{\mathrm{matrix}}$. In a material with $P6_3cm$ symmetry there are six equivalent directions $\langle 1\bar{1}0\rangle$. In the xy plane, this corresponds to the three possible directions $n=1,2,3$ of the crystallites shown in Fig. 3(a). The anisotropy of the SHG polarization $P_n^{\parallel}(2\omega)$ oriented parallel to the electric field $\vec{E}(\omega)$ of the incident light wave is shown in Fig. 3(b). $P_n^{\parallel}(2\omega)$ was derived from the tensor components for ferroelectrically induced SHG in Table I. Note that in the most general case,

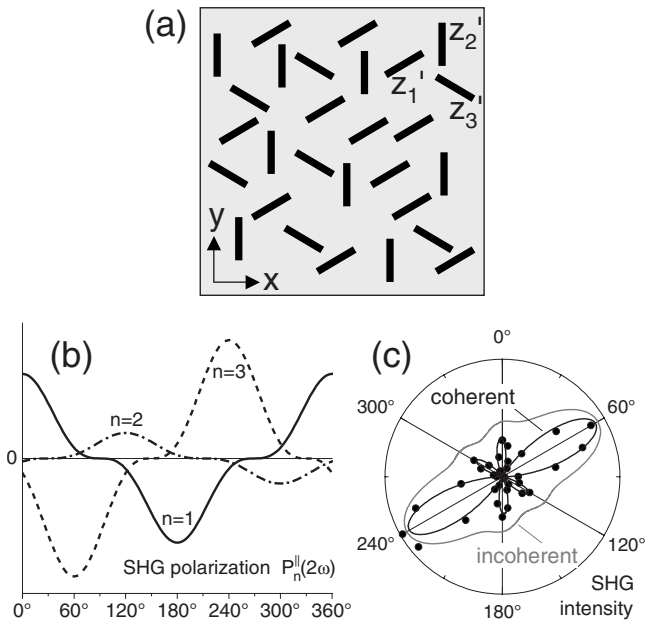

FIG. 3. Crystallographic inclusions and SHG intensity. (a) Sketch of the distribution of differently oriented ferroelectric $HoMnO_3$ nanoinclusions in the epitaxial z-oriented $HoMnO_3$ matrix. The local z_n' axes refer to the three possible orientations ($n=1,2,3$) of the local z axes of the inclusions in the xy plane of the film. (b) Anisotropy of the SHG polarization $P_n^{\parallel}(2\omega)$ for $n=1,2,3$ in the range of $0°-360°$. The different amplitudes of the polarization reflect the anisotropic distribution of inclusions with $n=1,2,3$ (see text). (c) Anisotropy of the SHG signal for the SHG polarization in (b) fitting coherent (black line) or incoherent (gray line) interference of the SHG contributions from different crystallites. Symbols are SHG data obtained from a $HoMnO_3$ film of 50 nm grown by MOCVD. The fit confirms the model of coherent interference.

the density of crystallites and, thus, the amplitude of $P_n^{\parallel}(2\omega)$ may differ with n.

The actual SHG intensity is given by $I_{\mathrm{SHG}}^{\parallel} \propto |P^{\parallel}(2\omega)|^2$, and here two cases must be distinguished.

1. Incoherent superposition

If the mean distance between two nanoinclusions is larger than the optical resolution of the detection system (here about 10 μm), contributions from neighboring inclusions will not interfere. In this case, the total SHG yield of a sample is given by $I_{\mathrm{SHG}}^{\parallel} \propto \Sigma_n |P_n^{\parallel}(2\omega)|^2$.

2. Coherent superposition

If the mean distance between two nanoinclusions is smaller than the optical resolution, contributions from neighboring inclusions will interfere. Here, the total SHG yield is given by $I_{\mathrm{SHG}}^{\parallel} \propto |\Sigma_n P_n^{\parallel}(2\omega)|^2$.

The anisotropy of the SHG signal for coherent and for incoherent interference of the contributions in Fig. 3(b) is shown in Fig. 3(c) and compared to the SHG data obtained on a $HoMnO_3$ film of 50 nm grown by MOCVD. Figure 3(c) clearly shows that coherent interference describes the experimental data well. As simulated in Fig. 3(b), the lobes associated to the $n=1,2,3$ orientation of the crystallites differ in size indicating that crystallites of different orientation are not equally distributed in this sample. Whereas the anisotropy of the SHG signal is at most varying slightly over the whole area of *one film*, differences become extensive when *different films* are compared. Here, Fig. 1(d) [respectively, Fig. 4(e)] and Fig. 3(c) were chosen as the end cases of a highly isotropic and a highly anisotropic distribution of crystallites. In Fig. 3(c), the density of inclusions with $n=3$ and $n=2$ differs by 4.6:1. A systematic relation between the degree of anisotropy and the growth technique or the film thickness was not found. Even for samples grown in succession, the degree of anisotropy can vary substantially. We thus conclude that the preference of a specific orientation of the crystallites must

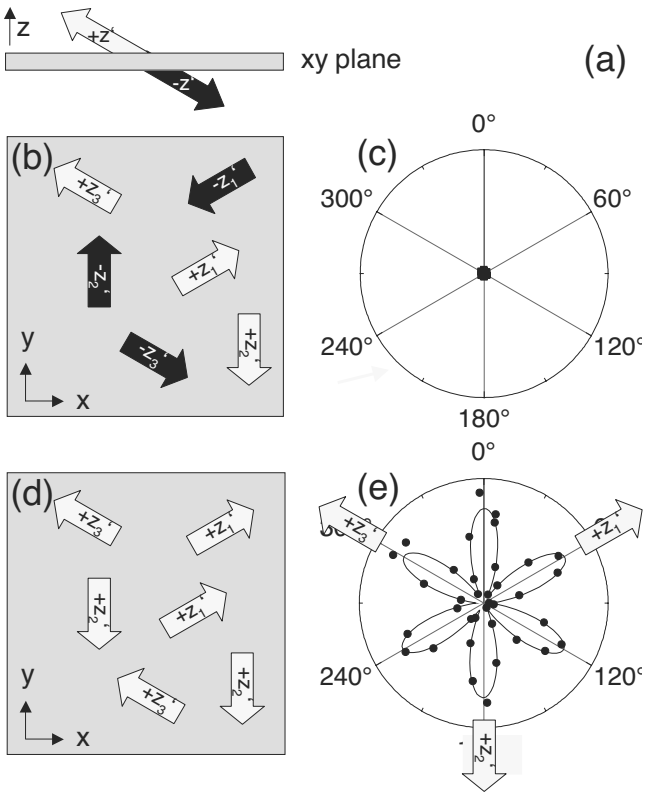

FIG. 4. Distribution of ferroelectric nanodomains. A sketch of the distribution of differently oriented ferroelectric $HoMnO_3$ nanoinclusions in the epitaxial z-oriented $HoMnO_3$ matrix along with the resulting intensity and anisotropy of the SHG signal are shown. In contrast to Fig. 3, the direction of the local polarization of the nanoinclusions ($+p$, white; $-p$, black) was taken into account. (a) z component of the polarization of the nanoinclusions in (b) and (d). (b) Sketch for equal distribution of nanoinclusions with $+p$ and $-p$. (c) The calculated SHG intensity for a distribution of nanoinclusions as in (b) cancels out, which is indicated by the dot at zero intensity. (d) Sketch for preferentially oriented polarization of the nanoinclusions, here along $+z_n'$. (e) Fit (solid line) of the SHG intensity for a distribution of nanoinclusions as in (d). SHG data (filled circles) obtained from a $HoMnO_3$ film of 100 nm grown by MOCVD confirm the scenario in (d) while disagreeing with panels (b) and (c). Note that unlike in Fig. 3, a fit and SHG data corresponding to an isotropic distribution of inclusions with $n=1,2,3$ were chosen for simplicity.

depend on very subtle effects that uniformly affect the whole film. Here, small variations in the growth process or of the substrate surface properties may be examples.

The SHG signal generated by the nanoinclusions is three orders of magnitude weaker than ferroelectric SHG obtained on a bulk crystal. Taking into account projection and interference effects in Fig. 3(a), the volume density of the inclusions is thus estimated as 10^{-3}. The HR-TEM images in Ref. 21 and in Fig. 2(a) show that the lateral expansion of the nanoinclusions is in the order of 10 nm. This corresponds to a mean distance of about 100 nm between the inclusions. Note that the sensitivity of the SHG experiment allows us to detect inclusions at volume densities lower than 10^{-5}, which exceeds the sensitivity of an x-ray-diffraction experiment by three orders of magnitude.

Thus far, we have not considered the direction of the spontaneous polarization in the nanoinclusions. As shown in Fig. 4, this polarization may be $+p$ or $-p$ with respect to the local z_n' axis of an inclusion with the orientation $n=1,2,3$. SHG contributions from oppositely oriented nanodomains cancel out because $\vec{P}^{(+p)}(2\omega)=-\vec{P}^{(-p)}(2\omega)$.[39] With coherent interference, the total SHG yield would, therefore, be zero if an equal distribution of nanodomains with $+p$ and $-p$, as in Fig. 4(b), was present. The SHG data in Fig. 4(e) show that the distribution of nanodomains is apparently *not* homogeneous. One set of nanodomains represented by white arrows in Fig. 4(b) prevails and leads to a nonzero SHG yield. A preferred direction of polarization of the nanoinclusions ($+z'$, respectively, $+p$ in our example) indicates that the isotropy of the $HoMnO_3$ film with respect to "up" ($+z$) and "down" ($-z$) is broken. This is the case if the direction of polarization in the epitaxial c-oriented $HoMnO_3$ matrix is also uniform, i.e., if the matrix forms a ferroelectric single-domain state. The SHG yield of the matrix supports this explanation. In comparison to a bulk sample with ferroelectric domains in the range of 1 μm, where destructive interference of SHG from neighboring domains is substantial,[39] the SHG yield from the films is up to four orders of magnitude higher. Moreover, ferroelectric domain walls as in Ref. 39 were not observed in spatially resolved SHG measurements on the films which confirms that they adopt a single-domain state.

C. Size and distribution of antiferromagnetic domains in RMnO$_3$ films

Relating the SHG signal observed on the RMnO$_3$ films to the ferroelectric order leaves the question why no antiferromagnetic contribution to the SHG signal is detected on any of the films investigated here. Two scenarios may account for this absence.

In the first scenario, the lateral size of the antiferromagnetic domains d may be much smaller than in a bulk crystal. As in the case of ferroelectric SHG, the contributions from opposite domains are phase-shifted by 180° with respect to each other: $\vec{P}^{(+\ell)}(2\omega)=-\vec{P}^{(-\ell)}(2\omega)$ with ℓ as antiferromagnetic order parameter. This results in destructive interference, if the lateral size d of the domains is lower than the optical resolution s of the detection system.[39]

In preparatory experiments, we determined $s\approx 10$ μm independent of the choice of digital camera or photo multiplier tube as light detector. If all domains have exactly the same size, forming a two-dimensional checkerboard pattern as in Ref. 39, the SHG signal drops rapidly to zero once $d<s$. However, in realistic samples, domains have a mean-lateral size $\bar{d}$ varying by σ_d. Because of the resulting local statistical imbalance in the distribution of $+\ell$ and $-\ell$ domains, the cancellation of SHG at $d<s$ is retarded. As derived elsewhere,[40] one finds

$$\frac{I_{\mathrm{SHG}}}{I_{\mathrm{SHG}}^0}=4\left(\frac{\sigma_d}{\bar{d}}\right)^2\left(\frac{\bar{d}}{s}\right)^2, \tag{2}$$

with I_{SHG}^0 as unattenuated SHG intensity of a single-domain sample. Using $\sigma_d/\bar{d}\approx 1$ on the basis of images of antiferromagnetic $YMnO_3$ bulk domains[41] and assuming that apart from their larger size the topology is similar to that in the films, we find that for $\bar{d}>150$ nm a detectable SHG signal would be obtained. Thus, 150 nm is the upper threshold for the mean-lateral extension of the antiferromagnetic domains in the RMnO$_3$ films. From the width of the magnetic diffraction lines in recent neutron-scattering experiments,[25] coherence lengths of 65 nm (z) and 20 nm (x) for films of 500 nm thickness with R=Y,Ho,Er were derived which is consistent with our threshold for the antiferromagnetic domain size.

The reduced domain size may be a consequence of magnetostriction in the films. In Refs. 42 and 43, it was shown that the magnetization inherent to an antiferromagnetic domain wall may interact with local strain via the piezomagnetic effect. This can reduce the free energy so that massive formation of domain walls becomes energetically favorable. Strain is imposed by the substrate and also by the misoriented nanoinclusions formed throughout the film. Alternatively, growth-induced antiphase boundaries may pose a limit to the expansion of the antiferromagnetic domains, thus restricting their size.

In the second scenario, a ferroelectric single-domain state is known to induce rare-earth ferromagnetism and a transition of the manganese sublattice to the magnetic symmetry $P6_3\underline{cm}$ in bulk $HoMnO_3$.[5] For this symmetry, SHG with light incident along the z axis is also not allowed.

Experiments on $YMnO_3$ films point to the first scenario because here, too, an antiferromagnetic SHG contribution is not observed, but the polarization-induced transition to the magnetic $P6_3\underline{cm}$ state does not occur. In $HoMnO_3$, the second scenario may apply *in addition* to the first scenario but since the SHG signal is, in any case, zero, this cannot be verified here.

IV. CONCLUSION

The ferroelectric and the antiferromagnetic structure of epitaxial hexagonal RMnO$_3$ films with R=Y,Dy,Ho,Er were characterized on nanoscopic length scales by optical SHG. The formation of ferroelectric nanoinclusions with secondary orientations with respect to the c axis of the epitaxial film matrix was observed in all films, irrespective of growth technique and film thickness. The volume density of the in-

clusions is in the range of 10^{-3} and an estimate yields a mean distance on the order of 100 nm. The inclusions behave as nanodomains with a preferred direction of spontaneous polarization whereas the epitaxial *c*-oriented matrix forms a ferroelectric single-domain state. Antiferromagnetic domains possess a mean-lateral size of <150 nm, which is attributed to strain and antiphase boundaries. Indications for a polarization-induced magnetic order, different from that observed on bulk samples in a ferroelectric multidomain state, were discussed.

The most surprising aspect of this investigation is that in a textbook multiferroic with relatively high-ordering temperatures and a well-defined phase diagram, the ferroelectric, as well as the magnetic order, experience drastic modifications when changing from bulk crystals to thin films. The differences between the bulk and the film properties of the hexagonal $R\mathrm{MnO}_3$ system are most prominent at nanoscopic length scales between ~ 50 nm and 1 μm. Even when the film thickness approaches "bulklike" dimensions, no approach to the bulk properties of the multiferroic order is observed.

These results are relevant for the technological aspects of the magnetoelectric effect in multiferroics because, here, the transfer from bulk crystals to thin films is almost mandatory and magnetoelectric coupling effects are known to depend critically on the size and distribution of domains. Our observations show onto which aspects attempts to optimize the magnetoelectric coupling effects in multiferroics have to be focused, and the extraordinary sensitivity of SHG to deviations from the ideal bulk structure will be very useful in monitoring any development in this direction.

ACKNOWLEDGMENTS

Work at the University of Bonn and at LMPG-CNRS was supported by the STREP MaCoMuFi (NMP3-CT-2006-033221) of the European Community. Subsidy by the SFB 608 and the FOR 520 of the DFG is appreciated. The authors thank G. van Tendeloo and O. Lebedev from EMAT, Antwerpen, for the HR-TEM image.

[1] M. Fiebig, J. Phys. D **38**, R123 (2005).
[2] W. Eerenstein, N. D. Mathur, and J. F. Scott, Nature (London) **442**, 759 (2006).
[3] T. Kimura, Annu. Rev. Mater. Res. **37**, 387 (2007).
[4] T. Kimura, T. Goto, H. Shintani, K. Ishizaka, T. Arima, and Y. Tokura, Nature (London) **426**, 55 (2003).
[5] T. Lottermoser, T. Lonkai, U. Amann, D. Hohlwein, J. Ihringer, and M. Fiebig, Nature (London) **430**, 541 (2004).
[6] R. Ramesh and N. A. Spaldin, Nature Mater. **6**, 21 (2007).
[7] B. Lorenz, A. P. Litvinchuk, M. M. Gospodinov, and C. W. Chu, Phys. Rev. Lett. **92**, 087204 (2004).
[8] S. Lee, A. Pirogov, M. Kang, K. H. Jang, M. Yonemura, T. Kamiyama, S. W. Cheong, F. Gozzo, N. Shin, H. Kimura, Y. Noda, and J. G. Park, Nature (London) **451**, 805 (2008).
[9] T. Lonkai, D. G. Tomuta, U. Amann, J. Ihringer, R. W. A. Hendrikx, D. M. Többens, and J. A. Mydosh, Phys. Rev. B **69**, 134108 (2004).
[10] C. J. Fennie and K. M. Rabe, Phys. Rev. B **72**, 100103(R) (2005).
[11] P. Coeuré, F. Guinet, J. C. Peuzin, G. Buisson, and E. F. Bertaut, in *Proceedings of the International Meeting on Ferroelectricity*, edited by V. Dvorák (Institute of Physics of the Czechoslovak Academy of Sciences, Prague, 1966), pp. 332–340.
[12] N. Fujimura, T. Ishida, T. Yoshimura, and T. Ito, Appl. Phys. Lett. **69**, 1011 (1996).
[13] E. F. Bertaut and M. Mercier, Phys. Lett. **5**, 27 (1963).
[14] W. C. Koehler, H. L. Yakel, E. O. Wollan, and J. W. Cable, Phys. Lett. **9**, 93 (1964).
[15] M. Fiebig, D. Fröhlich, K. Kohn, S. Leute, T. Lottermoser, V. V. Pavlov, and R. V. Pisarev, Phys. Rev. Lett. **84**, 5620 (2000).
[16] E. F. Bertaut and J. Mareschal, C. R. Hebd. Seances Acad. Sci. **257**, 867 (1963).
[17] N. Iwata and K. Kohn, J. Phys. Soc. Jpn. **67**, 3318 (1998).
[18] B. Lorenz, F. Yen, M. M. Gospodinov, and C. W. Chu, Phys. Rev. B **71**, 014438 (2005).
[19] A. A. Bosak, C. Dubourdieu, J.-P. Sénateur, O. Y. Gorbenko, and A. R. Kaul, J. Mater. Chem. **12**, 800 (2002).
[20] A. A. Bosak, C. Dubourdieu, J.-P. Sénateur, O. Y. Gorbenko, and A. R. Kaul, Cryst. Eng. **5**, 355 (2002).
[21] I. E. Graboy, A. A. Bosak, O. Y. Gorbenko, A. R. Kaul, C. Dubourdieu, J.-P. Sénateur, V. L. Svetchnikov, and H. W. Zandbergen, Chem. Mater. **15**, 2632 (2003).
[22] J. H. Lee, P. Murugavel, D. Lee, T. W. Noh, Y. Jo, M. H. Jung, K. H. Jang, and J. G. Park, Appl. Phys. Lett. **90**, 012903 (2007).
[23] J.-H. Lee, P. Murugavel, H. Ryu, D. Lee, J. Y. Jo, J. W. Kim, H. J. Kim, K.-H. Kim, Y. Jo, M.-H. Jung, Y. H. Oh, Y. W. Kim, J.-G. Yoon, J.-S. Chung, and T. W. Noh, Adv. Mater. **18**, 3125 (2006).
[24] P. Murugavel, J.-H. Lee, D. Lee, T. W. Noh, Y. Jo, M.-H. Jung, Y. S. Oh, and K. H. Kim, Appl. Phys. Lett. **90**, 142902 (2007).
[25] I. Gélard, C. Dubourdieu, S. Pailhès, S. Petit, and C. Simon, Appl. Phys. Lett. **92**, 232506 (2008).
[26] J.-W. Kim, K. Dörr, K. Nenkov, and L. Schultz, J. Appl. Phys. **101**, 09M108 (2007).
[27] K. R. Balasubramaniam, S. Havelia, P. A. Salvador, H. Zheng, and J. F. Mitchell, Appl. Phys. Lett. **91**, 232901 (2007).
[28] J. Fontcuberta, B. Martínez, A. Seffar, S. Piñol, A. Roig, E. Molins, X. Obradors, J. Alonso, and J. M. González-Calbet, J. Appl. Phys. **79**, 5182 (1996).
[29] N. D. Mathur and M. Bibes, Philos. Mag. Lett. **87**, 139 (2007).
[30] J. Dho, C. W. Leung, J. L. MacManus-Driscoll, and M. G. Blamire, J. Cryst. Growth **267**, 548 (2004).
[31] C. Dubourdieu, G. Huot, I. Gélard, H. Roussel, O. I. Lebedev, and G. van Tendeloo, Philos. Mag. Lett. **87**, 203 (2007).
[32] J.-W. Kim, L. Schultz, K. Dörr, B. B. van Aken, and M. Fiebig, Appl. Phys. Lett. **90**, 012502 (2007).
[33] R. W. Boyd, *Nonlinear Optics* (Academic, New York, 1991).
[34] M. Fiebig, V. V. Pavlov, and R. V. Pisarev, J. Opt. Soc. Am. B

22, 96 (2005).
[35] P. S. Pershan, Phys. Rev. **130**, 919 (1963).
[36] R. R. Birss, *Symmetry and Magnetism* (North-Holland, Amsterdam, 1966).
[37] C. Degenhardt, M. Fiebig, D. Fröhlich, T. Lottermoser, and R. V. Pisarev, Appl. Phys. B: Lasers Opt. **73**, 139 (2001).
[38] J.-W. Kim, K. Nenkov, L. Schultz, and K. Dörr, J. Magn. Magn. Mater. **321**, 1727 (2009).
[39] M. Fiebig, D. Fröhlich, T. Lottermoser, and M. Maat, Phys. Rev. B **66**, 144102 (2002).
[40] The derivation is based on a statistical analysis on the distribution of domain size and will be published separately. Although the variable $\bar{d}$ cancels in Eq. (2), it is retained in order to express Eq. (2) in dimensionless quantities. The dependence of I_{SHG} on the domain size manifests as dependence on σ_d.
[41] M. Fiebig, J. Appl. Phys. **83**, 6560 (1998).
[42] A. V. Goltsev, R. V. Pisarev, T. Lottermoser, and M. Fiebig, Phys. Rev. Lett. **90**, 177204 (2003).
[43] B. Hanamura, K. Hagita, and Y. Tanabe, J. Phys.: Condens. Matter **15**, L103 (2003).